CO_2-based hollow-core fiber Raman laser with high-pulse energy at 1.95 µm

YAZHOU WANG,[1,†,*] OLAV THORBJØRN SANDBERG SCHIESS,[1,†] RODRIGO AMEZCUA-CORREA,[2] AND CHRISTOS MARKOS[1,3,*]

[1]*DTU Fotonik, Technical University of Denmark, DK-2800 Kgs. Lyngby, Denmark*
[2]*CREOL, The College of Optics and Photonics, University of Central Florida, Orlando, FL-32816, USA*
[3]*NORBLIS IVS, Virumgade 35D, DK-2830 Virum, Denmark.*
[†]*Equal contribution.*
**Corresponding authors: yazwang@fotonik.dtu.dk; chmar@fotonik.dtu.dk*

Received XX Month XXXX; revised XX Month, XXXX; accepted XX Month XXXX; posted XX Month XXXX (Doc. ID XXXXX); published XX Month XXXX

In this letter, we present a high pulse energy Raman laser at 1946 nm wavelength directly pumped with a 1533 nm custom-made fiber laser. The Raman laser is based on the stimulated Raman scattering (SRS) in an 8-meter carbon dioxide (CO_2) filled nested anti-resonant hollow-core fiber (ARHCF). The low energy phonon emission combined with the inherent SRS process along the low-loss fiber allows the generation of high pulse energy up to 15.4 µJ at atmospheric CO_2 pressure. The Raman laser exhibits good long-term stability and low relative intensity noise (RIN) of less than 4%. We also investigate the pressure-dependent overlap of the Raman laser line with the absorption band of CO_2 at 2 µm spectral range. Our results constitute a novel and promising technology towards high energy 2 µm lasers.

https://doi.org/10.1364/OL.99.099999

Development of high energy and narrow linewidth fiber lasers at 2 µm wavelength has attracted significant research and commercial attention due to their use in different applications such as gas detection, optical parametric oscillator, material processing, laser surgery, etc. [1–4]. Thulium and holmium doped fibers based on population inversion are widely used for this purpose [5,6]. However, the detrimental nonlinear effects (e.g., stimulated Brillouin/Raman scattering, nonlinear spectrum broadening), amplified spontaneous emission (ASE) and thermal damage limit their performance towards narrow linewidth and high-pulse energy [7–9]. The advent of gas-filled hollow-core fiber (HCF) Raman laser technology provides an alternative solution [10–12]. This laser architecture relies on gas as the active gain medium, thus offers important advantages such as low nonlinearity and high damage threshold, while the relatively high threshold of SRS can effectively suppress the ASE frequency conversion [11,13–18]. Within the HCF family, emerging silica ARHCFs can overcome the high silica loss at ultraviolet and infrared regions by confining most of the laser beam within its hollow-core region with extremely low overlap with the surrounding glass structure [19–21]. Several reports have demonstrated 2 µm high-energy Raman laser generation by filling hydrogen (H_2) into ARHCF, where the vibrational SRS was used for 2 µm laser conversion from a pump around 1 µm [10,11,22]. However, the use of high pressure hydrogen (H_2) adds an extra limitation of implementing these lasers in practical applications requiring portability. Furthermore, the use of H_2 introduces not only high permeability of silica over long time periods [23], but also a high amount of heat release because of the long vibrational Stokes shift coefficient (4155 cm^{-1}), inducing thus a significant long term drift of the Raman laser [24]. The aforementioned challenges can be addressed by utilizing SRS through the rovibrational Q-branch of ν_1 band of the $\nu_1/2\nu_2$ Fermi dyad of CO_2 [25,26]. This is because its relatively low Stokes shift coefficient of 1385 cm^{-1} allows the direct generation of 2 µm laser from the 1.5 µm spectral range. Moreover, the remarkably narrow Raman gain linewidth (~ 300 MHz at 1 bar) formed by Dicke narrowing and collisional line-mixing effect is an important advantage for the development of ultra-narrow linewidth lasers [27]. Recently, a near-infrared (near-IR) frequency comb has been demonstrated based on cascaded SRS in a CO_2-filled ARHCF using a 1064 nm Nd:YAG pump laser [28]. The cascaded SRS leads to the formation of a weak 3rd order Stoke line at 1911 nm driven by the 2nd Stoke at 1510 nm. Although the intensity of the 3th order Stokes line is quite low due to the cascaded configuration and the long CO_2 molecule dephasing time relative to the pump pulse duration of ~450 ps, this work confirms that 2 µm laser can be achieved directly from a 1.5 µm pump.

In this letter, we demonstrate a high-energy CO_2-filled ARHCF Raman Stoke line at 1946 nm. The pump is a linearly

polarized fiber laser at 1533 nm, with ~92 μJ pulse energy, ~60 pm linewidth, 8 kHz repetition rate, and 7 ns pulse duration [29]. The ARHCF used, shown in Fig. 1(a), has a nested structure, forming a hollow core region with diameter of ~37.6 μm [12]. The wall thickness and diameter are 406 nm and 22.2 μm for the outer capillaries, 621 nm and 6.04 μm for the nested (inner) capillaries, respectively. Our calculations indicated that, this structure enables a wide transmission in the near-IR while having high loss in the mid–infrared (mid-IR), as shown in Fig. 1(b). The combination of these two characteristics support the 1st order Raman conversion while blocking the higher order Stokes lines. Since the higher order Stokes are blocked, this allows the confinement of the full pulse energy in the 1st order line. Our calculations of the fiber transmission properties were performed as described in [18] and the loss at 1.53 μm and 1.95 um were found to be ~0.008 dB/m and ~0.35 dB/m, respectively.

Figure 1(c) presents a schematic of our experimental setup. The ARHCF is sealed by two gas cells that can accommodate a maximum CO_2 pressure of 20 bar. The fiber length is 8 m and it was coiled with a bend radius of ~15 cm. The pump laser is coupled into the ARHCF with a coupling efficiency of ~80%. A half-wave plate (HWP) was used to optimize the pump polarization direction and therefore the SRS efficiency. The collimated output from the ARHCF passes through a CaF_2 dispersive prism, to spatially separate the Raman laser from the residual pump, and to allow the simultaneous characterization of both lasers. A flip mirror is used in front of the prism for the laser's spectral characterization using an optical spectrometer (Spectro 320, Instrument Systems). The pulse profiles of the residual pump and Raman laser are respectively detected by a 5 GHz near-IR photodetector (DET08C/M, Thorlabs) and a 100 MHz mid-infrared photodetector (PDAVJ10, Thorlabs). The beam profiles are measured with a slit scanning beam profiler (BP109- IR2, Thorlabs).

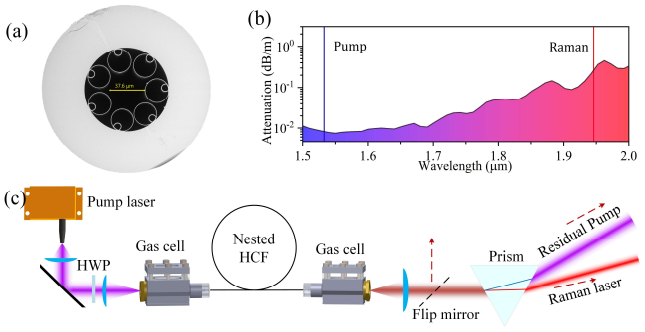

Figure 1. (a) Scanning electron microscopy image of the ARHCF. (b) Calculated fiber loss of the ARHCF using finite element method with COMSOL software. (c) Experimental setup for the generation of the 1.94 μm Raman laser.

By properly setting the orientation of the HWP, a strong Raman laser with pulse energy of 15.3 μJ is directly measured at atmospheric pressure and maximum pump power. According to the measured optical spectrum in Fig. 2(a), the laser has a center wavelength of 1946 nm. Inset of Fig. 2(a) shows a zoom of the measured spectrum in the range of 1850 nm to 2050 nm. It can be seen that the spectrum has high purity since the ASE is left on the pump wavelength region. Given the ~60 pm pump linewidth, the Stokes shift coefficient of 1385 cm^{-1}, and the ~300 MHz Raman gain linewidth, our laser is estimated to be within the order of ~100 pm. This value exceeds the spectral resolution limit (0.2 nm) of our spectrometer and thus it cannot be accurately resolved. When the pressure in the CO_2-filled ARHCF increases over the range 1 to 17 bar, we found that the pulse energy already reaches the maximum level of 16.3 μJ (corresponding to 28 % quantum efficiency) at 1.2 bar, and then rapidly decreases, as shown in Fig. 2 (b). This tendency is different from other reported gas-filled ARHCF Raman lasers [29,30], where the pulse energy keeps increasing as the pressure increases, reaching eventually a saturation level [31]. The different trend in our experiment is attributed to the overlapping of the generated laser with the CO_2 absorption band, as indicated in Fig. 2(a). The increase of the gas pressure inside the ARHCF fiber leads to the increase of the Raman gain bandwidth (due to the reduced gas molecule dephasing time) and consequently the laser linewidth [32], meanwhile it broadens the absorption linewidth of the CO_2 gas due to the enhanced molecule collisions. As a result, the overlap between the Raman laser line and CO_2 absorption line increases with the increase in the gas pressure. This was experimentally verified by investigating the direct CO_2 absorption of the Raman laser by passing the collimated laser beam through a gas chamber filled with pure CO_2 at different pressures. The inner space of the gas chamber has a hollow cylindrical shape providing a 20 cm long optical path. Both ends of the chamber are sealed by two CaF_2 windows for gas filling. An infrared photodetector was used for recording the pulse peak intensity. Figure 2 (c) shows the direct absorption of CO_2 under different pressure (inside the chamber), where the Raman laser used for the absorption measurement was generated under a constant 10 bar pressure inside the ARHCF, to guarantee a relatively large laser linewidth and therefore enable a high CO_2 absorption. It can be seen that, when the CO_2 pressure inside the gas chamber increases from 1 to 15 bar, the peak intensity of our laser shows a corresponding decrease. When the CO_2 inside the chamber is replaced by pure argon, the peak intensity becomes independent of the pressure, further verifying the absorption effect of the CO_2. It should be noted that the signal fluctuation observed in our measurements originates from the quantum noise which acts as a seed for the SRS and we will discuss later. We also recorded the variation of the pulse peak intensity at atmospheric pressure, but at different CO_2 concentrations. The different concentrations were controlled using two different mass flow controllers with argon as diluting gas. Our measurements however did not reveal any observable difference on the peak intensity, indicating the negligible absorption influence of CO_2 on the Raman laser at atmospheric pressure. Figure 2(d) shows the measured Raman pulse energy versus the coupled pump pulse energy at the optimal CO_2 pressure of 1.2 bar. When the pump pulse energy exceeds the SRS threshold of ~50 μJ, the energy shows almost a linear increase, reaching the maximum value of 16.3 μJ.

Figure 2(e) shows the impact of the pressure inside the CO2-filled ARHCF on the pulse profiles of both the Raman laser and the residual pump. Three Raman and corresponding

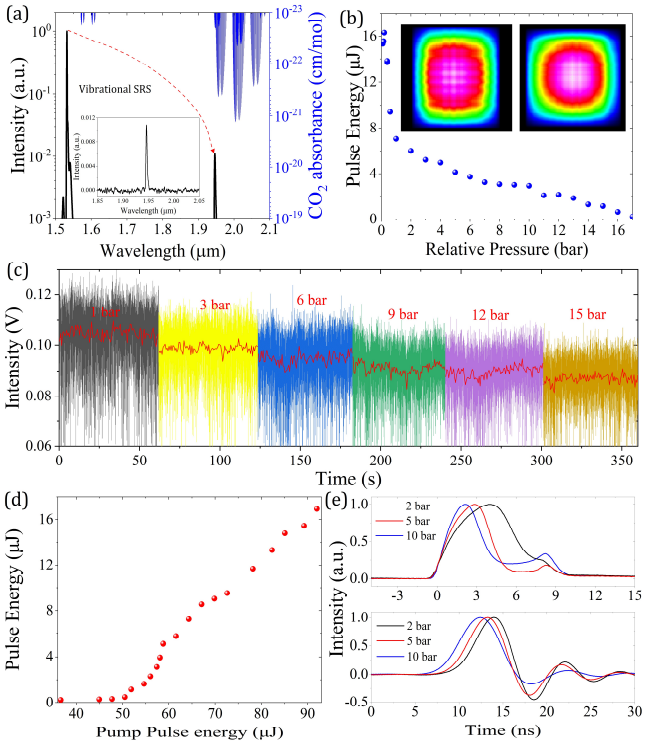

Figure 2. (a) The left axis shows the measured spectrum including both the residual pump and Raman laser. The right axis includes the absorption spectrum of CO_2 obtained from the high resolution transmission molecular absorption database. Inset of (a) is a zoomed spectrum. (b) Raman pulse energy versus the CO_2 pressure. Insets of (b) are measured beam profiles of the Raman laser (left) and the residual pump (right). (c) Measured pulse peak intensities of the Raman laser after passing through a 20 cm long gas chamber at different CO_2 pressures. (d) Raman laser pulse energy measurements versus pump pulse energy. (e) Average of 10000 pulses at different pressures for residual pump (top) and Raman laser (bottom).

residual pump pulse profiles at different pressure levels are provided for comparison. Each pulse profile is an average of 10000 measured pulses. To facilitate the comparison, the average power of these three Raman lasers are fixed to 4.4 mW by properly adjusting the input pump power. The power coupling into the detector is precisely controlled by neutral density filters, to ensure that most of the laser pulses lies in the linear detection regime of the photodetector [24,33]. When the pressure increases from 2 to 10 bar, due to the suppression of the transient SRS regime, the residual pump pulse duration on top of Fig. 2(e) rapidly decreases from 5.3 ns to 3.0 ns, and a second peak gradually appears in the trailing edge region [30]. The trailing edge of the Raman pulses (bottom of Fig. 2(e)) exhibits an oscillation due to the 100 MHz bandwidth limitation of the mid-IR photodetector. It can be seen that the oscillation intensity reduces with the increase of the pressure, indicating the increase of the Raman pulse duration. The decrease of the residual pump and the increase of the Raman pulse duration respectively at high pressure case are attributed to the associated decrease in molecular dephasing time, which is a crucial index for measuring the transition time from spontaneous Raman scattering to SRS state [34,35].

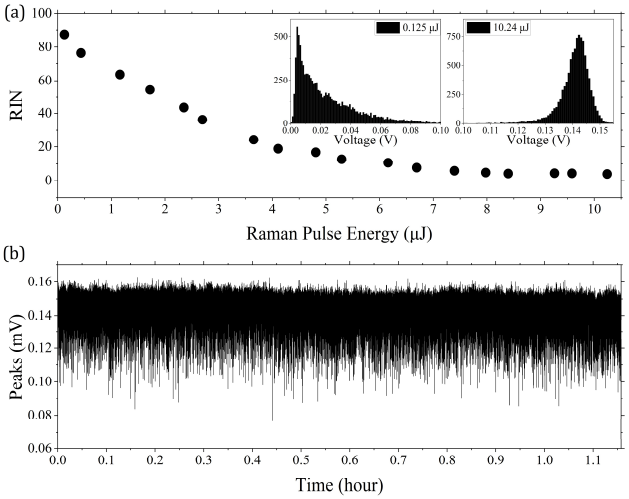

Figure 3. (a) RIN of the Raman laser measured at different pulse energies. Insets of (a) are histograms of peak intensity distributions of a 0.125 μJ (left) and a 10.2 μJ (right) pulse energy. (b) 200000 Raman laser peaks measured at maximum Raman power over ~1.2 hour to show long-term stability.

Another important observation is that the center part of the residual pump pulse profile at 10 bar is higher than the one at 5 bar. This is a sign that the Raman laser suffers from a higher CO2 absorption loss at higher pressures, which is consistent with our deduction in Fig. 2(c) and further verifies our initial assumption.

Since the SRS process is initiated by the random quantum noise, one can claim that the Raman lasers have in general a relatively high pulse-to-pulse fluctuation [36]. Here we use RIN (defined as the ratio of the standard deviation to the mean value of the pulse peak intensity) to describe the noise performance of our laser. Figure 3(a) shows the measured RIN of the Raman pulse peak intensity as a function of pulse energy. Each RIN value is counted based on 10000 pulses. Initially, the RIN is up to 87% at a low pulse energy of 0.125 μJ. The RIN decreases with an increase of the average pulse energy, and then stabilizes at a minimum level of ~4% when the energy is higher than ~8 μJ. Insets of Fig. 3(a) present the statistical distribution of the pulse peak intensity at two different average pulse energy levels. One can see that the distribution has a negative exponential distribution at a low energy of 0.125 μJ which reflects the behavior of quantum noise [36,37], and, due to the depletion of the pump power as well as the CO_2 molecules in the ground state during the SRS [38], it becomes a Gaussian-like distribution as the pulse energy increases. These effects are found to be consistent with the conventional free-space (gas chambers) Raman laser as well as with our recent work based on a H_2-filled ARHCF [24,36,37].

It is worth to emphasize that heat effect has been found to be a limiting factor to the performance of gas-filled ARHCF lasers [24]. A high amount of heat released during the SRS can significantly compromise the long-term stability of the laser [24,33]. In this work, due to the small photon energy difference between the pump and Raman Stokes, the maximum pulse energy of 16.3 μJ is associated with a heat release of only 4.4 μJ, therefore the laser exhibits a good long-term stability without

significant drift for more than 1 hour, as shown in Fig. 3 (b). Note that this measurement was recorded after 2 hours warming-up of the laser system, in order to stabilize the pump laser and the coupling efficiency from the pump to the ARHCF.

In conclusion, we demonstrate that CO_2 can act as an efficient Raman active medium for frequency conversion from ~1.5 μm to ~2 μm using the ARHCF technology. We present that our approach has specific advantages over other configurations, and we report a maximum Raman pulse energy of 16.3 μJ at a gas pressure of only 0.2 bar above atmospheric pressure. The RIN of the laser reaches a minimum level (4%) when the energy of the laser exceeds ~8 μJ. Due to the low amount of heat release within the CO_2-filled ARHCF, the laser has a good long-term stability without any significant drift. Given the usual gain range of Er-doped fiber from ~1530 to ~1610 nm, the wavelength of the CO_2-filled fiber Raman laser could be easily extended to the range of ~1941 - ~2072 nm, therefore constituting a promising way towards high energy 2 μm laser generation.

Funding. This work is supported by the Danmarks Frie Forskningsfond Hi-SPEC project (Grant No. 8022-00091B), VILLUM FONDEN (Grant No. 36063), LUNDBECK FONDEN (Grant NO. 71293), and US ARO (Grant No. W911NF-19-1-0426).

Disclosures. The authors declare no conflicts of interest, and declare that the copyright belongs to the authors.

References

1. K. Scholle, S. Lamrini, P. Koopmann, and P. Fuhrberg, Front. Guid. Wave Opt. Optoelectron. (2010).
2. R. Lewicki, G. Wysocki, A. A. Kosterev, and F. K. Tittel, Appl. Phys. B **87**(1), 157–162 (2007).
3. A. M. Heidt, J. H. V Price, C. Baskiotis, J. S. Feehan, Z. Li, S. U. Alam, and D. J. Richardson, Opt. Express **21**(20), 24281–24287 (2013).
4. M. Gebhardt, C. Gaida, P. Kadwani, A. Sincore, N. Gehlich, C. Jeon, L. Shah, and M. Richardson, Opt. Lett. **39**(5), 1212–1215 (2014).
5. M. Meleshkevich, N. Platonov, D. Gapontsev, A. Drozhzhin, V. Sergeev, and V. Gapontsev, CLEO/Europe and IQEC 2007 Conference Digest (Optical Society of America, 2007), p. CP2_3.
6. S. D. Jackson, A. Sabella, A. Hemming, S. Bennetts, and D. G. Lancaster, Opt. Lett. **32**(3), 241–243 (2007).
7. A. Yeniay, J.-M. Delavaux, and J. Toulouse, J. Light. Technol. **20**(8), 1425 (2002).
8. H. Jiang, L. Zhang, and Y. Feng, Opt. Lett. **40**(14), 3249–3252 (2015).
9. X. Tian, X. Zhao, M. Wang, and Z. Wang, Opt. Lett. **45**(17), 4802–4805 (2020).
10. A. V. Gladyshev, A. N. Kolyadin, A. F. Kosolapov, Y. P. Yatsenko, A. D. Pryamikov, A. S. Biryukov, I. A. Bufetov, and E. M. Dianov, Quantum Electron. **45**(9), 807–812 (2015).
11. Z. Wang, B. Gu, Y. Chen, Z. Li, and X. Xi, Appl. Opt. **56**(27), 7657–7661 (2017).
12. A. I. Adamu, Y. Wang, M. S. Habib, M. K. Dasa, J. E. Antonio-Lopez, R. Amezcua-Correa, O. Bang, and C. Markos, Opt. Lett. **46**(3), 452–455 (2021).
13. C. Markos, J. C. Travers, A. Abdolvand, B. J. Eggleton, and O. Bang, Rev. Mod. Phys. **89**(4), 45003 (2017).
14. F. Benabid, J. C. Knight, G. Antonopoulos, and P. S. J. Russell, Science **298**(5592), 399–402 (2002).
15. F. Couny, F. Benabid, and P. S. Light, Phys. Rev. Lett. **99**(14), 143903 (2007).
16. F. Benabid, F. Couny, J. C. Knight, T. A. Birks, and P. S. J. Russell, Nature **434**(7032), 488–491 (2005).
17. L. Cao, S. Gao, Z. Peng, X. Wang, Y. Wang, and P. Wang, Opt. Express **26**(5), 5609–5615 (2018).
18. Y. Chen, Z. Wang, B. Gu, F. Yu, and Q. Lu, Opt. Lett. **41**(21), 5118–5121 (2016).
19. M. S. Habib, J. E. Antonio-Lopez, C. Markos, A. Schülzgen, and R. Amezcua-Correa, Opt. Express **27**(4), 3824 (2019).
20. M. Klimczak, D. Dobrakowski, A. N. Ghosh, G. Stępniewski, D. Pysz, G. Huss, T. Sylvestre, and R. Buczyński, Opt. Lett. **44**(17), 4395–4398 (2019).
21. A. I. Adamu, M. S. Habib, C. R. Petersen, J. E. A. Lopez, B. Zhou, A. Schülzgen, M. Bache, R. Amezcua-Correa, O. Bang, and C. Markos, Sci. Rep. **9**(1), 4446 (2019).
22. A. V Gladyshev, A. N. Kolyadin, A. F. Kosolapov, Y. P. Yatsenko, A. D. Pryamikov, A. S. Biriukov, I. A. Bufetov, and E. M. Dianov, Laser Phys. **27**(2), 25101 (2016).
23. N. Kurita, N. Fukatsu, H. Otsuka, and T. Ohashi, Solid State Ionics **146**(1), 101–111 (2002).
24. Y. Wang, A. I. Adamu, M. K. Dasa, J. E. Antonio-Lopez, M. S. Habib, R. Amezcua-Correa, O. Bang, and C. Markos, J. Light. Technol. **39**(11), 3560–3567 (2021).
25. J. Baran, A. Grofcsik, and W. J. Jones, Mol. Phys. **45**(6), 1291-1297 (1982 (n.d.) .
26. B. Lavorel, G. Millot, R. Saint‐Loup, H. Berger, L. Bonamy, J. Bonamy, and D. Robert, J. Chem. Phys. **93**(4), 2176–2184 (1990).
27. D. Xiong, Y. Bai, D. Zuo, and X. Wang, J. Raman Spectrosc. **52**(4), 857-864 (2021).
28. K. Krupa, K. Baudin, A. Parriaux, G. Fanjoux, and G. Millot, Opt. Lett. **44**(21), 5318–5321 (2019).
29. Y. Wang, M. K. Dasa, A. I. Adamu, J. E. Antonio-Lopez, M. S. Habib, R. Amezcua-Correa, O. Bang, and C. Markos, Opt. Lett. **45**(7), 1938–1941 (2020).
30. A. V. Gladyshev, A. F. Kosolapov, M. S. Astapovich, A. N. Kolyadin, A. D. Pryamikov, M. M. Khudyakov, M. E. Likhachev, and I. A. Bufetov, "Efficient 4.42 μm Raman laser based on hollow-core silica fiber," arXiv:1801.01729 (2018).
31. W. K. Bischel and M. J. Dyer, J. Opt. Soc. Am. B **3**(5), 677 (1986).
32. W. K. Bischel and M. J. Dyer, Phys. Rev. A **33**(5), 3113–3123 (1986).
33. A. I. Adamu, M. S. Habib, C. R. Smith, J. E. Antonio Lopez, P. Uhd Jepsen, R. Amezcua-Correa, O. Bang, and C. Markos, Sci. Rep. **10**(1), 4912 (2020).
34. R. L. Carman, F. Shimizu, C. S. Wang, and N. Bloembergen, Phys. Rev. A **2**(1), 60–72 (1970).
35. M. G. Raymer and J. Mostowski, Phys. Rev. A **24**(4), 1980–1993 (1981).
36. M. G. Raymer and I. A. Walmsley, E. B. T.-P. in O. Wolf, ed. (Elsevier, 1990), 28, pp. 181–270.
37. E. Landahl, D. Baiocchi, and J. R. Thompson, Opt. Commun. **150**(1), 339–347 (1998).
38. I. A. Walmsley, M. G. Raymer, T. Sizer, I. N. Duling, and J. D. Kafka, Opt. Commun. **53**(2), 137–140 (1985).